

Model-Based Resolution:

Applying the Theory in Quantitative Microscopy

Andrés Santos[†], Ian T. Young[§]

[†] Escuela Técnica Superior de Ingenieros de Telecomunicacion, Universidad Politécnica de Madrid,

E-28040 Madrid, Spain

e-mail: andres@die.upm.es Tel. +34 91 336 68 27 Fax: +34 91 336 73 23

[§] Department of Applied Physics, TU Delft, NL-2628 CJ Delft, The Netherlands

e-mail: young@ph.tn.tudelft.nl

Keywords: model-based measurement, optical resolution, quantitative microscopy, genomic distance

ABSTRACT

Model-based image processing techniques have been proposed as a way to increase the resolution of optical microscopes. In this paper, a model based on the microscope's Point Spread Function (PSF) is analyzed and the resolution limits achieved with a proposed goodness-of-fit criterion are quantified. Several experiments have been performed to evaluate the possibilities and limitations of this method: a) experiments with an ideal (diffraction limited) microscope, b) experiments with simulated dots and a real microscope, c) experiments with real dots acquired with a real microscope. The results show that a threefold increase over classical resolution (e.g. Rayleigh) is possible.

These results can be affected by model mis-specifications while model corruption, as seen in the effect of Poisson noise, seems to be unimportant. This work can be considered as preliminary with the final goal being the accurate measurement of various cytogenetic properties, such as gene distributions, in labeled preparations.

1. INTRODUCTION

The purpose of this work is to analyze the possibilities and limitations of model-based techniques to increase the resolution of two-dimensional, digital images acquired through optical microscopes. It is a first study in a work whose final goal is the measuring of the distance between genes in interphase nuclei and determining their gene distribution [1]. This problem could, in principle, have diagnostic implications as the information of whether two particular genes are on the same chromosome (and consequently at a fixed distance) could have clinical interpretation. This justifies the effort to obtain higher resolution with conventional (widefield) optical microscopes instead of using the more complex and expensive confocal microscopes.

To know the gene location in the nuclei, fluorescence probes are hybridized to individual genes and analyzed as dots whose presence and relative location in the acquired images are the relevant information. We, therefore, intend to measure the distances between two observable dots that represent the fluorescence light coming from two gene probes that have been appropriately hybridized. The relative peak intensities of the dots will also be measured.

In this paper, we will assume that the two fluorescence dots produce incoherent light as they originate from two distinct self-luminous light sources. Although this is only partially true for high-aperture microscope objectives, the study of partially coherent light sources is left for future work.

1.1. Model-based resolution

Although there are some classical definitions of optical resolution (such as that of Rayleigh) that consider only diffraction effects in a lens, according to van den Bos, the resolution limit depends actually on the errors in the observed intensity distributions [2, 3].

Following [2], the two-point resolution—the resolution of two superimposed and overlapping component intensity distributions—can be formulated as a two-component functional model-fitting to error–corrupted observations with respect to the locations and amplitudes of both components.

Then the two-component model can be defined as:

$$g(x, y/\mathbf{a}, \mathbf{b}) = \mathbf{a}_1 h(x - \mathbf{b}_{x1}, y - \mathbf{b}_{y1}) + \mathbf{a}_2 h(x - \mathbf{b}_{x2}, y - \mathbf{b}_{y2}) \quad \text{Eq. 1}$$

where $\mathbf{a} = (\mathbf{a}_1, \mathbf{a}_2)$ are the amplitudes, $\mathbf{b} = (\mathbf{b}_{x1}, \mathbf{b}_{x2}, \mathbf{b}_{y1}, \mathbf{b}_{y2})$ the peak locations of both components, and $h(x, y)$ is the component distribution. This equation can also be expressed as:

$$g(x, y/\mathbf{a}, \mathbf{b}, \mathbf{g}) = \mathbf{a}_0 \{ \mathbf{g} h(x - \mathbf{b}_{x1}, y - \mathbf{b}_{y1}) + (1 - \mathbf{g}) h(x - \mathbf{b}_{x2}, y - \mathbf{b}_{y2}) \} \quad \text{Eq. 2}$$

with γ as the peak ratio $\mathbf{g} = \mathbf{a}_1 / (\mathbf{a}_1 + \mathbf{a}_2)$ and $\mathbf{a}_0 = \mathbf{a}_1 + \mathbf{a}_2$.

Throughout this work, this model will be fitted to the error–free or noise–corrupted observations, trying to minimize the least squares criterion. The observations can include systematic errors (model mis-specification) and (in a well designed microscope) non-systematic or stochastic (Poisson noise) errors.

2. DOT LOCATION PROCEDURE

Keeping in mind the problem of locating fluorescence dots in cytogenetic applications, it will be assumed that a basic tool for a first rough location of the dots is already available. Perhaps a simple thresholding method will be used or more elaborate tools as described in [4-6]. The purpose of the work presented here is to refine this initial guess. A decision has to be made as to whether each of the dots located is actually one or two dots. In the two-dimensional projection of the three dimensional reality, one dot could be “hiding” behind a second one. If two dots are located close to one another, then their distance and peak ratio have to be measured as accurately as possible.

2.1. Building the model

The observation model has been obtained by approximating the microscope's point spread function (PSF) by an analytical function. As shown in Figure 1, two different kinds of mathematical functions have been tested—a Bessel-based model and a Gaussian-based model.

The 1-D Bessel model for a single dot is:

$$h(x) = p_1 \left(\frac{J_1(p_2(x - p_3))}{(x - p_3)} \right)^2 \quad \text{Eq. 3}$$

where $J_1(\bullet)$ is a Bessel function of the first kind and p_1 , p_2 and p_3 are the model parameters.

The 1-D Gaussian model for a single dot is:

$$h(x) = p_1 \exp\left(-p_2(x - p_3)^2\right) \quad \text{Eq. 4}$$

The 2-D model is obtained by simply evaluating these functions on a 2-D grid.

The Bessel model was chosen because in an ideal, aberration-free microscope, the lens diffraction produces a circularly symmetric PSF that follows this expression. (See section 3.1.) The Gaussian model was selected as it is simpler, faster to compute, and under many circumstances an excellent approximation to the Bessel model [7]. It should be noted, however, that although both models fit the PSF's central peak, the actual PSF is broader. The effects of this mismatch will be discussed in section 3.2.

2.2. One-dot and two-dot models:

The 2-D one-dot Bessel model is based on the expression:

$$d = \sqrt{(x - t_2)^2 + (y - t_3)^2}$$

$$\text{model}_1 = t_1 \left(\frac{J_1(p_2 d)}{d} \right)^2 \quad \text{Eq. 5}$$

and the 2-D two-dot Bessel model on the expression:

$$d_1 = \sqrt{(x - t_2)^2 + (y - t_3)^2} \quad d_2 = \sqrt{(x - t_4)^2 + (y - t_5)^2}$$

$$\text{dot}_1 = \left(\frac{J_1(p_2 d_1)}{d_1} \right)^2 \quad \text{dot}_2 = \left(\frac{J_1(p_2 d_2)}{d_2} \right)^2 \quad \text{Eq. 6}$$

$$\text{model}_2 = t_1(t_6 \text{dot}_1 + (1 - t_6) \text{dot}_2)$$

The 2-D one-dot Gaussian model is based on the expression:

$$\text{model}_1 = t_1 \exp\left(-p_2(x - t_2)^2\right) \exp\left(-p_2(x - t_3)^2\right) \quad \text{Eq. 7}$$

and the 2-D two-dot Gaussian model on the expression:

$$\begin{aligned}
 \text{dot}_1 &= \exp\left(-\left(p_2(x-t_2)\right)^2\right)\exp\left(-\left(p_2(y-t_3)\right)^2\right) \\
 \text{dot}_2 &= \exp\left(-\left(p_2(x-t_4)\right)^2\right)\exp\left(-\left(p_2(y-t_5)\right)^2\right) \\
 \text{model}_2 &= t_1 \left(t_6 \text{dot}_1 + (1-t_6) \text{dot}_2\right)
 \end{aligned}
 \tag{Eq. 8}$$

where $\{t_1 \text{ to } t_6\}$ are the fitting parameters in every case.

It can be argued whether two models are required, as the one-dot model can be built from the two-dot model. As will be seen in the next sections, both models are needed to define a goodness-of-fit criterion that permits one to discriminate between one or two dots in the image. The two-dot model, having a greater number of parameters, always achieves a better fit.

2.3. Fitting the model to the observations

The fitting procedure first fits the one-dot model to the observations and then fits the two-dot model. The decision as to whether there is a single dot or two dots is one of the critical steps of the method and will be discussed later. The basic tool that is used to fit the model is the Matlab function `leastsq` (optimization toolbox), using the Levenberg-Marquardt method applied to the error function:

$$\begin{aligned}
 \text{one dot :} \quad \text{err}_1 &= \sum_{x,y=1}^N (\text{image_data}[x,y] - \text{model}_1[x,y])^2 \\
 \text{two dot :} \quad \text{err}_2 &= \sum_{x,y=1}^N (\text{image_data}[x,y] - \text{model}_2[x,y])^2
 \end{aligned}
 \tag{Eq. 9}$$

The MatLab default values are used except for the maximum number of iterations which was increased to 1,000. Although this maximum number of iterations was occasionally reached and consequently it could be assumed that a better fit could be obtained with more iterations, this number was not increased in order to simulate a more realistic computational situation where the optimization time cannot increase indefinitely.

The fitting procedure required four input values:

- the x and y coordinates of the initial location. Although in the first experiments this location was chosen randomly in the neighborhood of the one of the dots, it was thought that a more realistic selection was a position of maximum brightness in the image: this (possibly non-unique) position is probably not the exact location of the dot(s) in noisy images, but it is easy to locate in real images;
- an initial peak ratio (γ_o) for the two-dot model; $\gamma_o = 0.52$ in all the experiments, and;
- the size of the subimage to be considered for fitting. In all the experiments described here, 40 pixels from the initial location in all four directions were used. Again this is a parameter to simulate a real situation; a larger subimage (or the whole available image) could be used. But in a real case with a larger image, some disturbing factors (other dots for example) could be included. How large this subimage actually is, depends on the sampling density which, in our case, is $2 \times 22.28 = 44.56$ pixels/ μm when corrected for binning. (See section 3.2.)

The optimization procedure adjusts the following parameters:

- Location (x, y coordinates) of one or two peaks depending on the model used;
- Amplitude of the model, t_1 , and;
- Peak ratio in the two-peak model (g). This parameter was not optimized in den Dekker's work [8], but has proved useful.

The procedure has the following steps:

- a) Determination of the initial location for the fitting algorithm. It has been chosen in all the experiments as the position of the absolute brightness maximum in the subimage considered. If there are several points with the same maximum value, the one closest to the upper-left corner is chosen.
- b) Starting from the initial location, the one-dot model is fitted.
- c) Starting from the initial location, the two-dot model is fitted.

In the Den Dekker procedure [8] the two-dot fit starts from the saddle or minimum point of the error function located with the single-dot model. When starting from this local minimum in our application, however, the two-dot model fitting sometimes cannot escape. We have obtained better results starting the second fitting from another point nearby, for example, the initial location determined in step (a).

- d) A decision is made as to whether the best fit is the single-dot or the double-dot model: a goodness-of-fit criterion has to be computed. For the Gaussian model only, the resolution criterion proposed in [2] is also computed.

2.4. Goodness-of-fit criterion

The measure of the goodness of an individual fit that we use is the mean-square error (mse):

$$\text{mse} = \frac{1}{N^2} \sum \text{err}^2 \quad \text{Eq. 10}$$

where err is the error between the actual and the obtained values for each pixel and N^2 is the number of pixels analyzed. This parameter is the square of the discrepancy, which is used by some authors (e.g. [9]).

The increase in the number of parameters of the two-dot model implies that it always obtains better fits and lower mse values; there are simply more degrees-of-freedom. Thus the decision as to whether the one-dot or two-dot fits is to be preferred has to be based on a relative measure such as the decrease in the mse when going from the one-dot to the two-dot model:

$$\mathbf{x} = \frac{\text{mse}_2 - \text{mse}_1}{\text{mse}_2} \quad \text{Eq. 11}$$

with mse_2 and mse_1 being the mean-square error of the two-dot fit and the one-dot fit, respectively. If \mathbf{x} is not above a certain threshold, the two-dot fit is discarded. The selection of the optimal threshold is a key point that will be discussed in following sections. Figure 4, for example, will show the effect of two different thresholds.

3. EXPERIMENTS

Several experiments have been performed to evaluate the possibilities and limitations of this method:

- a) experiments with an ideal (diffraction limited) microscope
- b) experiments with simulated dots and a real microscope
- c) experiments with real dots acquired with a real microscope.

3.1. Ideal case (diffraction limited)

An ideal aberration-free microscope, where the only limiting factor is the diffraction in the lens, will have a circularly-symmetric PSF, given by:

$$\text{PSF}(r) = \text{constant} \left(2 \frac{J_1(ar)}{r} \right)^2 \quad \text{Eq. 12}$$

where $J_1(\bullet)$ was defined previously and $a = 2\delta NA/I$. For $NA = 1.3$ and $I = 600$ nm, as in the rest of the experiments described here, $a = 13.614 \mu\text{m}^{-1}$.

A simulation has been conducted on the ability of the fitting procedure to locate two dots in this ideal case where the PSF is known and the two dots are infinitesimally small. The only non-deterministic consideration has been the introduction of Poisson noise, as it is always present, due to the photon-counting effect.

3.1.1. Method

A set of artificial images has been constructed simulating the effect of two dots at different relative distances d (from 1 to 40 pixels). It is assumed that the dots are infinitesimally small so that the observed image is the addition of two overlapping PSFs. The actual peak ratio (γ) was kept constant at a value of 0.6 even when the initial estimate was $\gamma_o = 0.52$ as described above.

To include Poisson noise, the simulated images were modified with the Matlab function `Poisrnd` (statistics toolbox). The SNR (signal-to-noise ratio) in the noisy image was computed on the area used to fit the model, in these experiments, 81×81 pixels. To obtain a specific value of SNR, the image was multiplied by a factor before applying `Poisrnd` and later was divided by the same factor. In this way, the SNR was adjusted to a value of approximately 15 dB.

The simulation was done using as the PSF the function $(J_1(0.2898 \times d)/d)^2$ that includes unitless distances d (pixels). The multiplying factor 0.2898 which is used in subsequent experiments was found for a Zeiss microscope and determined experimentally by fitting equation 12 to the measured PSF shown in Figure 1. (See section 3.2.) For a distance $d = 1$, using equation 12 means an actual distance of:

$$r = \frac{0.2898}{a} = \frac{0.2898}{13.614 \mu\text{m}^{-1}} = 0.021 \mu\text{m} \quad \text{Eq. 13}$$

that is, a sampling density of $1/0.021 \mu\text{m} = 46.96$ pixels/ μm . This value differs slightly from the direct measurement of the sampling density (44.56 pixels/ μm) referred to in section 3.2.

3.1.2. Results

The results of the fitting procedure using the Bessel model are shown in Table 1 and in Figure 2. The second and third columns in Table 1 show the error in determining the relative distance and the peak ratio when there is no noise included in the simulated images. The remaining columns show the results of 12 experiments performed for each distance d including Poisson noise (SNR = 15.7 dB). Columns 4-8 show the raw results of the two-dot model fitting. For small and large distances, the fit is obviously incorrect and a local minimum in the error function has been found. In columns 9-13, the same results are shown, excluding cases where the goodness-of-fit criterion χ is below the threshold value of 0.1.

3.1.3. Discussion

For large distances ($d > 20$), the effect of the finite image size is evident. As a large amount of the intensity distribution of the second dot is left out of the image, the fit deteriorates. This effect cannot be considered of importance as—the distance being large—the initial dot location procedure would not have problems in detecting the presence of two dots. The single-dot fit then will improve the individual dots' locations, allowing accurate distance measurements.

For small distances ($d < 4$), the situation is different. Sometimes the procedure fails to locate both dots and this can be considered the resolution limit: $4 \times 0.021 \mu\text{m} = 0.084 \mu\text{m}$. It is interesting to note that the Rayleigh resolution limit in this case is $0.61\lambda / NA = 0.282 \mu\text{m}$. In this ideal case, there is a 3.3 improvement in resolution!

3.2. Simulated dots and real microscope

A step towards a more realistic case has been achieved using the data (PSF and pixel size) from a real microscope. In this case, using the experimentally-obtained PSF from a Zeiss Axioskop microscope (Zeiss Corporation, Jena, Germany), simulated images with one or two dots were "built." These dots were assumed to be point-like objects so the simulated image is either the PSF (one-dot images) or the overlap of two PSF functions in different locations and multiplied by different amplitude factors (two-dot images).

3.2.1 Equipment

The equipment selected was the same as the one used by Netten [4, 5]. In order to use his images as a test set, we used a Zeiss Axioskop microscope with a Photometrics KAF 1400 camera (Photometrics Corporation, Tucson, Arizona) using 2x2 binning. The objective was an oil-immersion 40x, NA=1.3 Zeiss Plan Neofluor.

The experimentally obtained sampling density (excluding binning) was known to be 5.57 pixels/ μm [10]. Considering the binning, this meant a sampling density of 2.785 pixels/ μm . The fluorescence emission wavelength was assumed to be 600 nm; actually it was 615 nm for the fluorochrome used but the OTF (optical transfer function) had been measured for 600 nm.

3.2.2. Obtaining the Model

The PSF was computed by taking the inverse Fourier transform of the one-dimensional, 256-point OTF that had been measured. As this method to measure the OTF uses a spatial interpolation by a factor of eight, the PSF is obtained in this 8x interpolated space [10]. To achieve greater accuracy, all the experiments have been done in this interpolated space. It should be kept in mind that in all of the

simulation experiments eight pixels in a simulated image are equivalent to one pixel in an actual (acquired) image. This yields a simulated sampling density of $8 \times 2.785 = 22.28$ pixels/ μm in the binned image from above which translates to 44.56 pixels/ μm in the unbinned image. Finally, two analytic models were built: a Gaussian-based and a Bessel-based one.

Gaussian-based model – The PSF was approximated by a Gaussian function with three parameters as given in equation 4. This fitting was done with the Matlab function `curvefit` (optimization toolbox) which uses the least squares method. Only parameter p_2 in equation 4 was actually used in the computations as the function was normalized to one and shifted to the origin. The equations shown in section 2.2 were used to build the one-dot and two-dot models.

The model shows a good fit in Figure 1 to the PSF's main lobe, although it does not account for the secondary lobes. These lobes are small and initially it was thought that they would not affect the location of the image peaks. This mismatch, however, has some effects as will be seen. The full width at half maximum (FWHM) of each peak in this Gaussian model is nine pixels while the full width at 10% of the maximum is 25 pixels.

Bessel-based model – The PSF was approximated by the three-parameter function given in equation 3. As in the previous case, the fitting of this equation to the microscope's PSF was done with the Matlab function `curvefit` and the 2-D model obtained by evaluating this expression on the 2-D grid.

3.2.3. Results from single-dot experiments

The accuracy of the location of individual dots was measured with a set of experiments with simulated images of a single dot. These images included Poisson noise with an average SNR of 15 dB as measured in the subimage.

From 71 cases analyzed with the Bessel model, the mean error in the location of the dot coordinates (x, y) measured in pixels in the interpolated space was $(-0.010, 0.006)$ and the standard deviation was $(0.054, 0.043)$. With the Gaussian model, 376 cases were studied, obtaining a mean error in the location of the dot coordinates of $(0.004, -0.005)$ with a standard deviation of $(0.051, 0.053)$. As a reference, the position of the brightness maximum in a dot image, when used as an estimate of the dot location, produced a mean error of $(0.085, 0.056)$ in the first 71 cases and of $(0.013, -0.040)$ in the 376 remaining ones with standard deviations of $(0.874, 0.924)$ and $(0.869, 0.855)$, respectively.

3.2.4. Results from two-dot experiments

Table 2 shows the results of the experiments with the Gaussian and the Bessel model. The cases where the goodness-of-fit criterion χ was not above a threshold value of 0.1 or 0.4 have been discarded as meaningless. When Poisson noise is included, the table shows the mean and standard deviations of several analyzed cases: 20 with the Gaussian model and 14 with the Bessel model. The columns with the label " n (%)" show the cases that have been included in the computations, thereby excluding the cases discarded by a low threshold value χ . The percentage of these cases with respect to the total simulations done is given in the parentheses. These results are also presented in Figures 3 and 4 with the former showing the Bessel model and the latter, the Gaussian model.

3.2.5. Discussion

Apart from the random variations due to the Poisson noise, there are some systematic errors that seem to be attributable to the lack of accuracy in the models used. Both the Gaussian and Bessel models, as can be seen in Figure 1, do not accurately follow the secondary lobes in the microscope PSF. This seems to be the reason for the following three effects:

Meaningless results at very short distances – At distances around five or fewer pixels, the fitting algorithm produces meaningless results. A second “ghost” dot is found at a distance around 14 pixels ($\gamma = 0.89$) for the Gaussian model, or 7 to 11 pixels for the Bessel model. This second dot is possibly due to the secondary lobes, not considered in the model. These incorrect fittings, however, can be detected by an appropriate threshold on the goodness-of-fit criterion χ .

Slight underestimation of distances when the dots are around 10 to 20 pixels apart – This seems to be due to an increase in the brightness amplitude of the neighboring peak produced by the secondary lobes. As this is something the model does not take into account, the best fit for each peak is moved slightly towards the other peak leading to an underestimate.

Small bias in the measure of peak ratios – The overlap of peaks means that each dot increases the amplitude of its neighbor. Thus there is some tendency to compensate with differences in their relative amplitudes. As again this is not modeled, there is a bias in the estimation of a peak ratio towards $g = 0.5$. To test if this was the real reason for the underestimation of the peak ratio, an experiment has been done with simulated images having true peak ratios of 0.5, 0.6, and 0.7. The results are shown in Figure 5 and confirm clearly the tendency to estimate a peak ratio of 0.5. Note that when γ is really 0.5, the error is negligible.

3.3. Real dots acquired with a real microscope

Experiments that used real fluorescence dot images instead of simulated images were also performed. Due to the difficulty in knowing the real distance and peak ratio between dots in acquired images, however, artificial images were constructed where an acquired dot was replicated at known distances and with known peak ratios.

The real cytogenetic images were extracted from the Netten test set [11] where the dots were centromeres labeled with a Spectrum Orange probe and acquired with a dual band-pass filter DAPI/O4 with an integration time of 1.0 s.

3.3.1. Model for acquired dots

It was assumed that the real dots that would be analyzed had a diameter of 1 μm . A model of a circularly symmetric dot of this diameter was then constructed. First, a 1-D model was obtained by convolving the 1-D PSF (see Figure 1) with a rectangular function whose width was equal to 1 μm or 22 binned pixels. The result of this convolution has a FWHM of 24 pixels and a full-width (FW) at 10% of the maximum of 44 pixels. A Gaussian model is then fit to this 1-D model. The parameter p_2 (as in equation 4) was then used to build the single-dot and the double-dot models.

3.3.2. Images used in the experiments

Two cytogenetic images with several nuclei were selected from the test set. In these eight-bit images, ten dots from six different cells were segmented with a mask created by a thresholding function

followed by five, eight-connected dilation operations (Matlab functions: `im2bw` and `dilate`.) The baseline intensity level (background plus nucleus intensity) was estimated with a bilinear interpolation from the four corner values in the dot's rectangular image (Matlab function `interp2`.) The values thus obtained were subtracted from the image. Finally the image was interpolated by eight using bicubic interpolation (Matlab function: `interp2`.)

The resulting dots were then analyzed with the standard procedure described above: fitting the single-dot and double-dot model. To give an idea of the sizes of the dots, the FWHMs measured on the two axes for each dot before and after interpolation are shown in Table 3.

Two types of images were created: images with a single dot and images with two dots. In the latter case in order to know the accuracy of the method in measuring inter-dot distances and peak ratios, the images were constructed by replicating a single dot at known distances and with a fixed peak ratio of $g = 0.6$.

3.3.3. Results with a single dot

For three of the ten dots, the two-dot model could be nevertheless fit to the single-dot images with significant results. Table 4 shows the results of this fit. To know whether the bicubic interpolation had any influence on these results, this analysis was repeated with the original (non-interpolated) dots that had been processed solely by segmentation and removal of the baseline. The results, also shown in Table 4, were very similar. The difference in the distance estimation is below one pixel in the interpolated space and the maximum difference in peak ratio is 0.02. The table shows that this double-dot fit is not due to the interpolation but to some feature present in the image.

3.3.4. Results with two (replicated) dots

The range where the distance could be estimated, the error in the distance, and the peak ratio measures are shown in Table 5. Two cases are delineated a) the results when discarding cases where $\xi < 0.4$ and b) results when discarding cases where $\xi < 0.6$.

3.3.5. Discussion

The experiments made with single dots suggest that the most critical point seems to be the resolution criterion. It seems that small asymmetries in the fluorescence probes mean that the double-dot model shows a good fit. It remains to be seen whether some of the acquired dots are actually two partially overlapping dots or a single one. As an example, *p8* seems a probable candidate to be a double dot. It is important to understand that the images analyzed were not from real gene probes but from much larger centromeric probes. A further study with controlled experiments involving real gene probes seems to be appropriate.

The resolution criterion described in [2] has been computed in all the experiments where the Gaussian model was used. In almost every case it showed that two point resolution was possible. The only exception was when testing an image with a single acquired dot, *p10*. In this case, when trying to fit the two-dot model, the obtained location for both dots was the same. The explanation of this is simple: with more parameters to adjust it is always possible to find a solution that mathematically gives a better fit.

4. Conclusions

Using model-based techniques the resolution limits have been increased in several cases to $3\times$ the resolution limit that one would expect from a classical definition such as the Rayleigh limit. The influence of Poisson noise (at the levels studied here) does not seem strong. More important is the influence of model mis-specifications. When real images are involved, however, biological factors such as the shape and size of the fluorescence dot images will have to be carefully considered.

Concerning the resolution decision, the goodness-of-fit criterion χ provides useful information. Further studies are needed to know its dependency on the SNR. Perhaps an adaptive threshold might be defined. It should take into account the level of the peak maxima as an estimation of the Poisson noise present in the image.

Finally, our assessment of the influence of g , the relative dot intensity, on the entire procedure must be extended. It is well-known, for example, that in interphase cells, the relative brightness of dots from homologous chromosomes can differ significantly [12]. A full study of the accuracy of the relative intensity measures is, therefore, under way.

ACKNOWLEDGMENTS

The work of Prof. Young was primarily sponsored by the Rolling Grants program of the Foundation for Fundamental Research in Matter (FOM) and the Delft Inter-Faculty Research Center Intelligent Molecular Diagnostic Systems (DIOC-IMDS).

5. REFERENCES

1. S. Dietzel, E. Weilandt, R. Eils, C. Münkler, C. Cremer, T. Cremer, "Three-dimensional distribution of centromeric or paracentromeric heterochromatin of chromosomes 1, 7, 15 and 17 in human lymphocyte nuclei studied with light microscopic axial tomography," *Bioimaging* **3**, 121-133 (1995).
2. A. Van den Bos, "Ultimate resolution: a mathematical framework," *Ultramicroscopy*, **47**, 298-306 (1992).
3. A. J. den Dekker and A. Van den Bos, "Resolution: A Survey," *J. Opt. Soc. Am. A*, **14**, 547-557 (1997).
4. H. Netten, I.T. Young, L.J. van Vliet, H.J. Tanke, H. Vrolijk, and W.C.R. Sloos, "FISH and Chips: Automation of Fluorescent Dot Counting in Interphase Cell Nuclei," *Cytometry*, **28**, 1-10 (1997).
5. H. Netten, L.J. van Vliet, L.J., H. Vrolijk, W.C.R. Sloos, H.J. Tanke, I.T. Young, "Fluorescent dot counting in interphase cell nuclei," *BioImaging*, **4**, 93-106 (1996).
6. C. Ortiz de Solórzano, A. Santos, I. Vallcorba, J.M. García-Sagredo. F. del Pozo, "Automated FISH Spot Counting in Interphase Nuclei: Statistical Validation and Data Correction," *Cytometry*, **31**, 93-99 (1998).
7. L.J. Van Vliet and P.W. Verbeek, "Better Geometric Measurements Based on Photometric Information," in Proceedings of the IEEE Conference on Instrumentation and Measurement Technology, S. Okamura, T. Nemoto, S. Fujimura, K. Watanabe, eds. (IEEE, Hamamatsu, Japan, 1994) pp. 1357-1360.
8. A. J. den Dekker, Model-based resolution, Ph. D. Thesis in Applied Physics. (Delft University of Technology, 1997).
9. W.F. Maddams, "The scope and limitations of curve fitting," *Applied Spectroscopy*, **34**, 245-267 (1980).
10. A. Klein, R. van den Doel, I.T. Young, S. Ellenberger, L.J. van Vliet, "Quantitative evaluation and comparison of light microscopes", in Proceedings of SPIE Conference on Optical Investigation of Cells In Vitro and In Vivo, D.L. Farkas, R.C Leif, B.J.Tromberg, eds. (SPIE, San Jose, California, 1998) pp. 162-173.
11. H. Netten, Automated Image Analysis of FISH-Stained Cell Nuclei, Ph. D Thesis (Delft University of Technology, 1997).
12. P. M. Nederlof, S. van der Flier, A. K. Raap, H. J. Tanke, "Quantification of inter- and intranuclear variation of fluorescence in situ hybridization signals," *Cytometry*, **13**, 831-838 (1992).

Table 1: Ideal case: diffraction limited microscope with two infinitesimally small objects. Results using the Bessel-based model: Δd is the difference between the obtained and the actual distances (in pixels in the interpolated space) and $\Delta \gamma$ is the difference between the obtained and the actual peak ratios. When Poisson noise is included, the table shows the mean and standard deviation over several simulated images. Three cases are presented: **a)** without noise (columns 2,3); **b)** Poisson noise included, 12 experiments (columns 4-8); **c)** the same as before, but discarding cases where $\xi < 0.1$ (columns 9-13). The column "n (%)" shows the number of cases included in the previous computations and the percentage these cases mean on the total of cases analyzed.

Actual distance	Without noise		Poisson noise; SNR ~15.7 dB					Poisson noise; SNR ~15.7 dB discarding when $\xi < 0.1$				
	Δd	$\Delta \gamma$	mean Δd	std Δd	mean $\Delta \gamma$	std $\Delta \gamma$	n (%)	mean Δd	std Δd	mean $\Delta \gamma$	std $\Delta \gamma$	n (%)
1	-0.02	0.006	2.90	3.42	0.246	0.163	12(100)	-	-	-	-	0 (0)
2	-0.01	0.002	1.40	1.81	0.184	0.147	12(100)	-	-	-	-	0 (0)
3	-0.01	0.001	0.27	0.43	0.072	0.117	12(100)	-	-	-	-	0 (0)
4	0.00	0.000	-0.03	0.27	-0.022	0.055	12(100)	-0.03	0.27	-0.022	0.055	12 (100)
5	0.00	0.000	0.09	0.18	0.006	0.037	12(100)	0.09	0.18	0.006	0.037	12 (100)
6	0.00	0.000	0.00	0.17	0.004	0.033	12(100)	0.00	0.17	0.004	0.033	12 (100)
7	0.00	0.000	0.08	0.15	0.009	0.015	12(100)	0.08	0.15	0.009	0.015	12 (100)
8	0.00	0.000	0.01	0.08	0.007	0.015	12(100)	0.01	0.08	0.007	0.015	12 (100)
9	0.00	0.000	-0.06	0.10	-0.001	0.009	12(100)	-0.05	0.10	-0.001	0.009	12 (100)
10	0.00	0.000	0.07	0.09	-0.001	0.009	12(100)	0.07	0.09	-0.001	0.009	12 (100)
11	0.00	0.000	0.01	0.08	0.000	0.006	12(100)	0.01	0.08	0.000	0.006	12(100)
12	0.00	0.000	0.00	0.07	-0.002	0.005	12(100)	0.00	0.07	-0.002	0.005	12(100)
13	0.00	0.000	-0.02	0.13	0.000	0.005	12(100)	-0.02	0.13	0.000	0.005	12(100)
14	0.00	0.000	0.03	0.10	0.002	0.006	12(100)	0.03	0.10	0.002	0.005	12(100)
15	0.00	0.000	0.01	0.07	-0.001	0.003	12(100)	0.01	0.07	-0.001	0.003	12 (100)
16	0.00	0.000	0.03	0.05	0.000	0.003	12(100)	0.03	0.05	0.000	0.003	12 (100)
17	0.00	0.000	0.04	0.12	0.002	0.004	12(100)	0.04	0.12	0.002	0.004	12 (100)
18	0.00	0.000	0.00	0.05	-0.001	0.005	12(100)	0.00	0.05	-0.001	0.005	12 (100)
19	0.00	0.000	0.00	0.11	0.000	0.004	12(100)	0.00	0.11	0.000	0.004	12(100)
20	0.00	0.000	-0.02	0.08	0.001	0.004	12(100)	-0.02	0.08	0.001	0.004	12 (100)
21	0.00	0.000	-1.56	0.23	0.012	0.042	12(100)	-0.04	0.08	0.000	0.004	11 (92)
22	0.00	0.000	-0.03	0.09	0.001	0.003	12(100)	-0.03	0.09	0.001	0.003	12 (100)
23	0.00	0.000	-4.44	8.06	0.068	0.142	12(100)	-0.03	0.09	0.000	0.002	9 (75)
24	0.00	0.000	-1.80	0.26	0.024	0.078	12(100)	-0.03	0.09	0.001	0.004	11 (92)
25	0.00	0.000	-3.81	8.84	0.029	0.083	12(100)	-0.03	0.18	0.028	0.086	10 (83)
26	0.00	0.000	-1.99	6.87	0.013	0.035	12(100)	-0.01	0.09	0.003	0.002	11 (92)
27	0.00	0.000	0.05	0.10	-0.001	0.003	12(100)	0.05	0.10	-0.001	0.003	12 (100)
28	0.00	0.000	-4.06	9.61	0.025	0.115	12(100)	0.01	0.09	0.000	0.004	10 (83)
29	0.00	0.000	-4.08	9.53	0.058	0.135	12(100)	-0.01	0.06	0.001	0.005	10 (83)
30	0.00	0.000	-16.13	14.33	0.069	0.154	12(100)	-0.01	0.04	0.000	0.006	5 (42)

Table 2: Experiment with two overlapping simulated dots and Gaussian and Bessel models (adjusted to the Zeiss Axioskop microscope). The table shows the error in the measured distances (Δd) and peak ratios ($\Delta \gamma$) for several cases. When Poisson noise is included, the table shows the mean (and standard deviation) over several simulated images, excluding the cases with low ξ . The column "n (%)" represents the number of cases considered to take the mean and standard deviation and the percentage these cases represent (how many have not been excluded by the parameter ξ).

Actual distance	Gaussian (no noise)		Gaussian model (Poisson noise; SNR ~13 dB)					Bessel (no noise)		Bessel model (Poisson noise; SNR ~13 dB)				
	discarding cases when $\xi < 0.1$		discarding cases when $\xi < 0.4$					discarding cases when $\xi < 0.1$		discarding cases when $\xi < 0.4$				
	Δd	$\Delta \gamma$	mean Δd	std Δd	mean $\Delta \gamma$	std $\Delta \gamma$	n (%)	Δd	$\Delta \gamma$	mean Δd	std Δd	mean $\Delta \gamma$	std $\Delta \gamma$	n (%)
4	6.61	0.236	-	-	-	-	0 (0)	3.37	0.086	-	-	-	-	0 (0)
5	3.08	0.118	-	-	-	-	0 (0)	2.42	0.003	-	-	-	-	0 (0)
6	2.04	0.027	-	-	-	-	0 (0)	2.01	-0.017	-	-	-	-	0 (0)
7	1.72	0.000	-	-	-	-	0 (0)	1.69	-0.023	-	-	-	-	0 (0)
8	1.50	-0.011	1.56	0.12	-0.005	0.010	19 (95)	1.41	-0.026	1.46	0.08	-0.026	0.006	14 (100)
9	1.30	-0.017	1.32	0.08	-0.019	0.007	20 (100)	1.15	-0.027	1.14	0.10	-0.029	0.007	14 (100)
10	1.11	-0.020	1.14	0.12	-0.019	0.006	20 (100)	0.90	-0.027	0.94	0.10	-0.028	0.006	14 (100)
11	0.91	-0.022	0.91	0.12	-0.023	0.007	20 (100)	0.66	-0.026	0.71	0.12	-0.028	0.007	14 (100)
12	0.71	-0.022	0.72	0.07	-0.023	0.008	20 (100)	0.43	-0.026	0.42	0.06	-0.026	0.004	14 (100)
13	0.51	-0.023	0.54	0.09	-0.024	0.005	20 (100)	0.20	-0.025	0.18	0.09	-0.026	0.006	14 (100)
14	0.32	-0.023	0.32	0.10	-0.023	0.005	20 (100)	-0.02	-0.024	-0.04	0.12	-0.024	0.006	14 (100)
15	0.13	-0.022	0.12	0.10	-0.020	0.005	20 (100)	-0.22	-0.023	-0.25	0.09	-0.021	0.005	14 (100)
16	-0.04	-0.022	-0.06	0.10	-0.022	0.005	20 (100)	-0.40	-0.022	-0.37	0.04	-0.020	0.005	14 (100)
17	-0.20	-0.021	-0.24	0.08	-0.021	0.003	20 (100)	-0.55	-0.021	-0.53	0.12	-0.022	0.004	14 (100)
18	-0.33	-0.020	-0.31	0.13	-0.021	0.004	20 (100)	-0.65	-0.019	-0.60	0.08	-0.019	0.004	14 (100)
19	-0.44	-0.019	-0.44	0.13	-0.019	0.003	20 (100)	-0.70	-0.018	-0.72	0.11	-0.020	0.006	14 (100)
20	-0.52	-0.018	-0.53	0.12	-0.017	0.004	20 (100)	-0.70	-0.017	-0.69	0.11	-0.016	0.004	14 (100)
21	-0.58	-0.017	-0.58	0.09	-0.016	0.005	20 (100)	-0.65	-0.016	-0.65	0.10	-0.014	0.005	14 (100)
22	-0.62	-0.016	-0.61	0.09	-0.016	0.004	20 (100)	-0.59	-0.014	-0.61	0.10	-0.015	0.006	14 (100)
23	-0.64	-0.015	-0.62	0.11	-0.016	0.004	20 (100)	-0.54	-0.013	-0.53	0.09	-0.013	0.005	14 (100)
24	-0.64	-0.014	-0.66	0.09	-0.013	0.005	20 (100)	-0.49	-0.012	-0.50	0.12	-0.012	0.005	14 (100)
25	-0.63	-0.013	-0.61	0.16	-0.013	0.004	20 (100)	-0.56	0.044	-0.49	0.15	-0.010	0.005	14 (100)
26	-0.61	-0.012	-0.61	0.11	-0.012	0.005	20 (100)	-0.53	0.045	-0.50	0.07	-0.009	0.003	14 (100)
27	-0.59	-0.011	-0.59	0.09	-0.010	0.004	20 (100)	-0.51	0.045	-0.48	0.10	-0.008	0.004	14 (100)
28	-0.57	-0.010	-0.57	0.11	-0.009	0.004	20 (100)	-0.50	0.048	-0.47	0.10	-0.008	0.005	14 (100)
29	-0.55	-0.009	-0.57	0.14	-0.008	0.003	20 (100)	-0.46	-0.008	-0.45	0.08	-0.006	0.004	14 (100)
30	-0.54	-0.007	-0.55	0.10	-0.006	0.004	20 (100)	-0.50	0.051	-0.42	0.15	-0.006	0.004	14 (100)
31	-0.53	-0.006	-0.55	0.12	-0.005	0.004	20 (100)	-0.43	0.052	-0.46	0.10	-0.005	0.004	14 (100)
32	-0.53	-0.005	-0.52	0.12	-0.004	0.005	20 (100)	-0.49	0.053	-0.46	0.14	-0.004	0.005	13 (93)
33	-0.53	-0.004	-0.51	0.10	-0.003	0.004	19 (95)	-0.63	0.054	-0.53	0.09	-0.004	0.005	14 (100)
34	-0.53	-0.002	-0.54	0.09	-0.002	0.005	19 (95)	-0.70	0.061	-0.55	0.15	-0.004	0.004	14 (100)
35	-0.52	-0.001	-0.51	0.15	0.001	0.003	16 (80)	-0.50	-0.001	-0.47	0.14	-0.002	0.005	12 (86)

Table 3: Full width at half maximum of the acquired dots used in the experiments, with and without cubic interpolation.

Dot Label	FWHM	FWHM
	without interpolation	with interpolation
<i>p1</i>	3 x 3	21 x 19
<i>p2</i>	3 x 3	24 x 18
<i>p3</i>	4 x 2	26 x 16
<i>p4</i>	3 x 3	19 x 18
<i>p5</i>	3 x 2	22 x 19
<i>p6</i>	3 x 2	24 x 19
<i>p7</i>	3 x 2	21 x 18
<i>p8</i>	6 x 4	42 x 20
<i>p9</i>	3 x 2	25 x 18
<i>p10</i>	2 x 2	17 x 16

Table 4: Results with a single (acquired) dot with and without interpolation: estimated distance, peak ratios and *goodness-of-fit* criterion for two-dot model fitting.

Dot Label	Interpolated case			Without interpolation		
	d	g	ξ	d	g	ξ
$p1$	20.99	0.87	0.37	2.70	0.88	0.30
$p2$	28.91	0.78	0.57	3.64	0.78	0.54
$p3$	13.69	0.70	0.25	1.62	0.71	0.22
$p4$	27.30	0.92	0.20	3.52	0.92	0.15
$p5$	27.20	0.89	0.18	3.51	0.90	0.15
$p6$	22.48	0.78	0.49	2.92	0.79	0.50
$p7$	24.48	0.85	0.34	3.09	0.86	0.38
$p8$	21.66	0.52	0.81	2.51	0.53	0.68
$p9$	16.08	0.79	0.35	2.01	0.81	0.28
$p10$	0.00	–	0.00	0.00	–	0.00

Table 5: Results with two (replicated) dots. ranges of the considered distance values and maximum error of the distance and peak ratio measurements in these ranges are shown for two cases: $\xi \geq 0.4$ and $\xi \geq 0.6$

Dot Label	Discarding cases when $\mathbf{x} < 0.4$			Discarding cases when $\mathbf{x} < 0.6$		
	Range(d)	max(Dd)	max(Dg)	Range(d)	max(Dd)	max(Dg)
$p1$	7-41	12.37	0.24	10-41	7.46	0.18
$p4$	13-48	1.78	0.04	15-48	1.72	0.03
$p5$	14-48	2.26	0.06	17-48	1.95	0.02
$p7$	11-41	10.18	0.19	17-41	1.20	0.06
$p10$	17-43	1.56	0.03	19-43	1.56	0.03
$p9$	8-37	8.49	0.19	17-37	0.99	0.03

FIGURE CAPTIONS

Figure 1: Bessel-based (above) and Gaussian-based (below) models. The models are shown as continuous lines (—) while the Zeiss Axioskop microscope PSF is shown as dashed line (••). The fitting was done as described in the text.

Figure 2: Results of the two-dot model fit in the ideal case. The simulated image is from an ideal diffraction-limited microscope considering Poisson noise. Left: Results of all fits obtained. Right: Discarding cases where $\xi < 0.1$. Note the different vertical scales.

Figure 3: Results of the experiments with simulated dots with the Bessel model for the Zeiss microscope parameters and including Poisson noise. Left: Discarding cases where $\xi < 0.1$. Right: Discarding cases where $\xi < 0.4$. Distances in pixels are in interpolated space. Note the different vertical scales.

Figure 4: Results of the experiments with simulated dots with the Gaussian model for the Zeiss microscope parameters and including Poisson noise. Left: Discarding cases where $\xi < 0.1$. Right: Discarding cases where $\xi < 0.4$. Distances in pixels are in interpolated space. Note the different vertical scales.

Figure 5: Simulated dots without noise. Error in the distance estimation and the peak ratio estimation for three values of the true peak ratio $\gamma = 0.7$ (above), $\gamma = 0.6$ (middle), and $\gamma = 0.5$ (below).

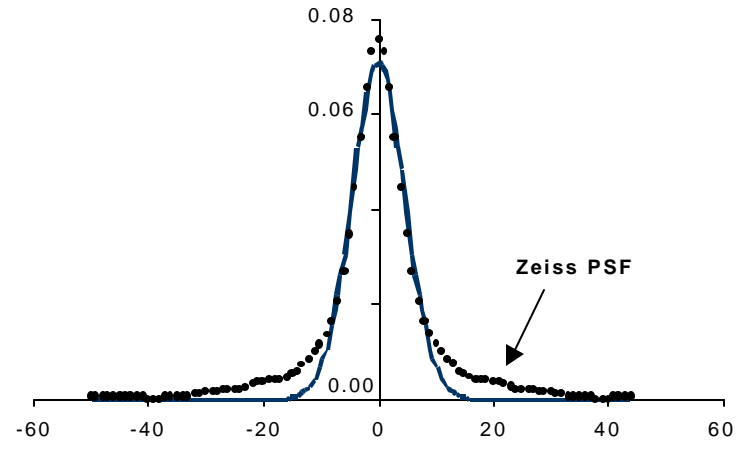
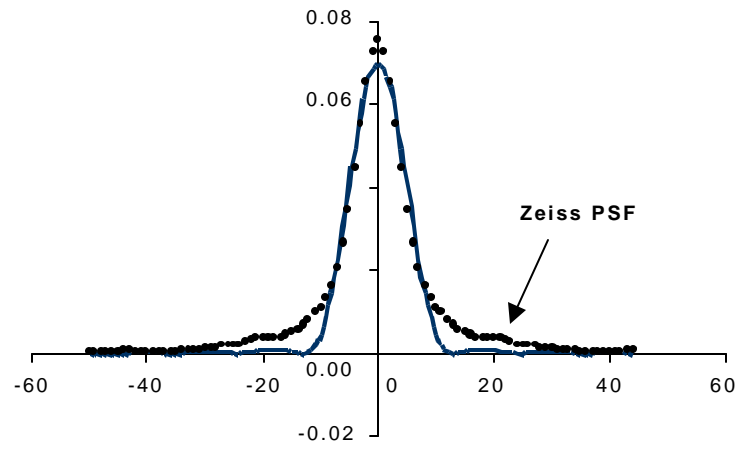


Figure 1: Bessel-based (above) and Gaussian-based (below) models. The models are shown as continuous lines (—) while the Zeiss Axioskop microscope PSF is shown as dashed line (••). The fitting was done as described in the text.

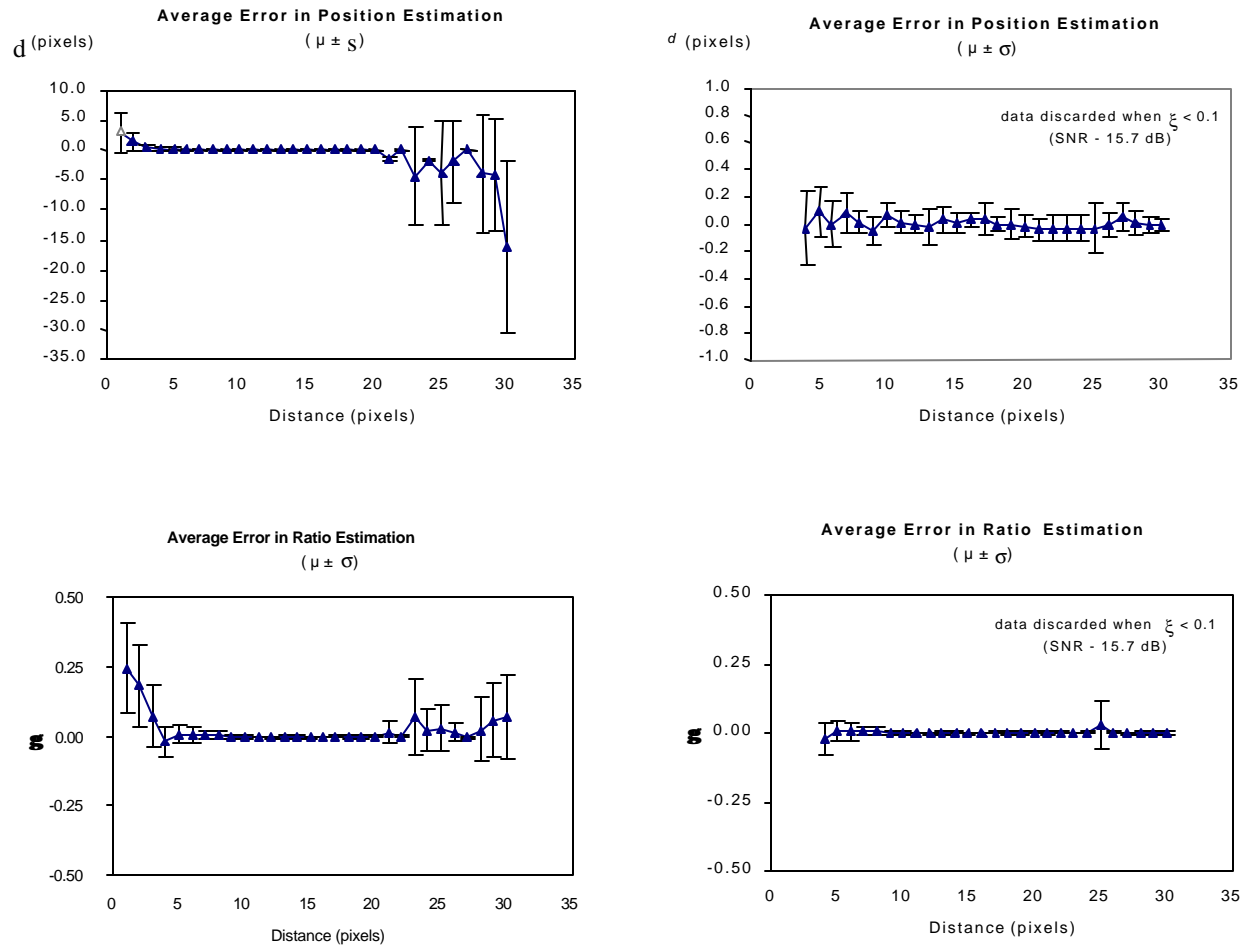


Figure 2: Results of the two-dot model fit in the ideal case. The simulated image is from an ideal diffraction-limited microscope considering Poisson noise. Left: Results of all fits obtained. Right: Discarding cases where $\xi < 0.1$. Note the different vertical scales.

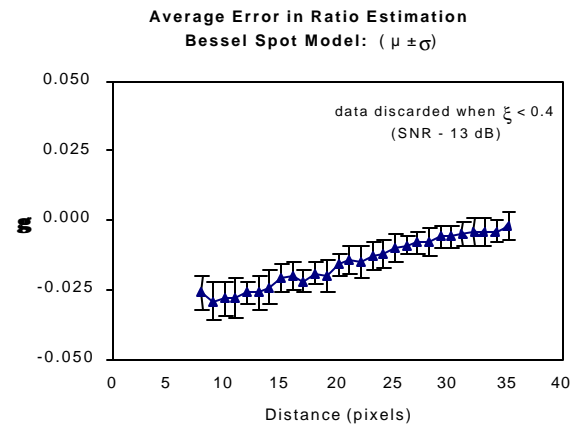
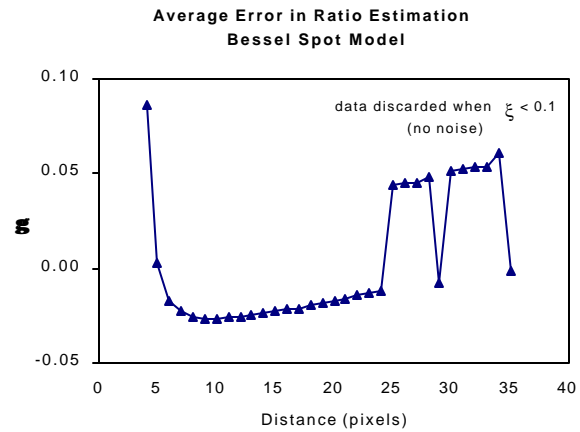
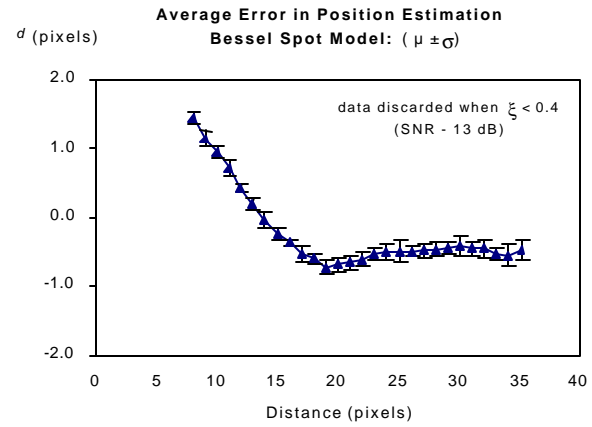
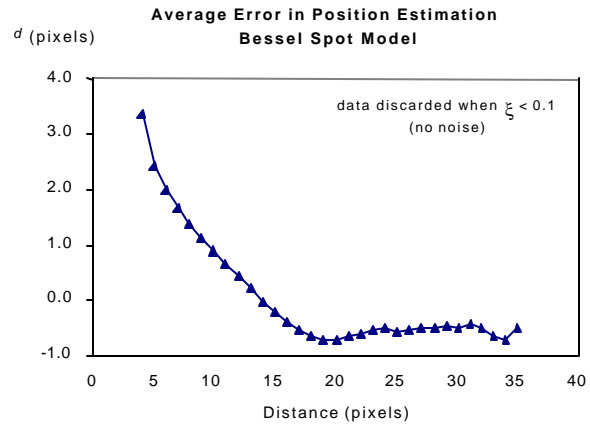
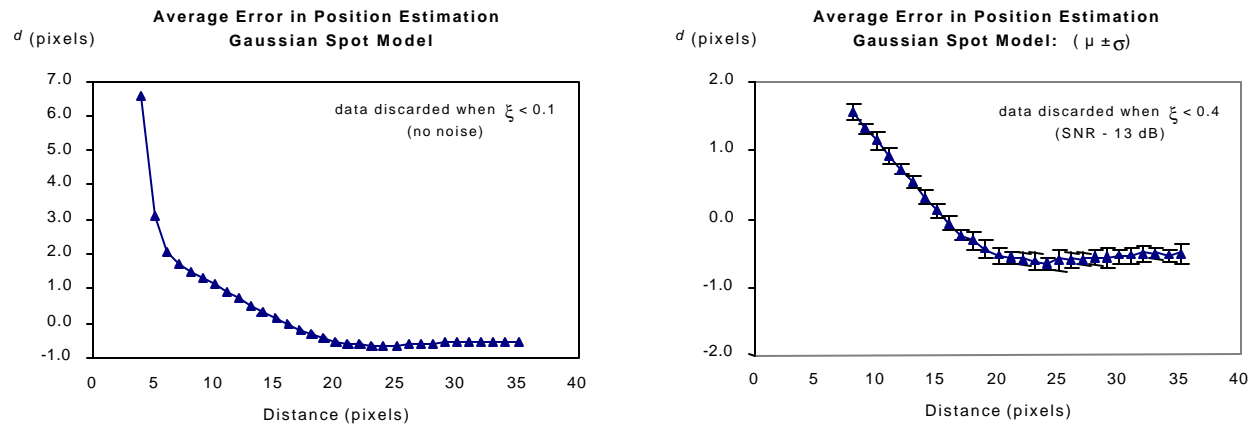


Figure 3: Results of the experiments with simulated dots with the Bessel model for the Zeiss microscope parameters and including Poisson noise. Left: Discarding cases where $\xi < 0.1$. Right: Discarding cases where $\xi < 0.4$. Distances in pixels are in interpolated space. Note the different vertical scales.



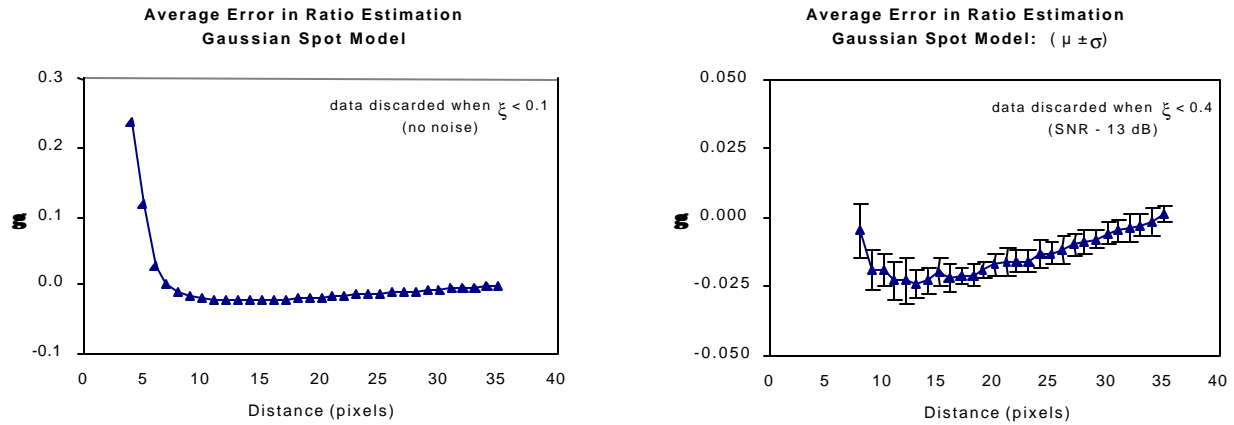
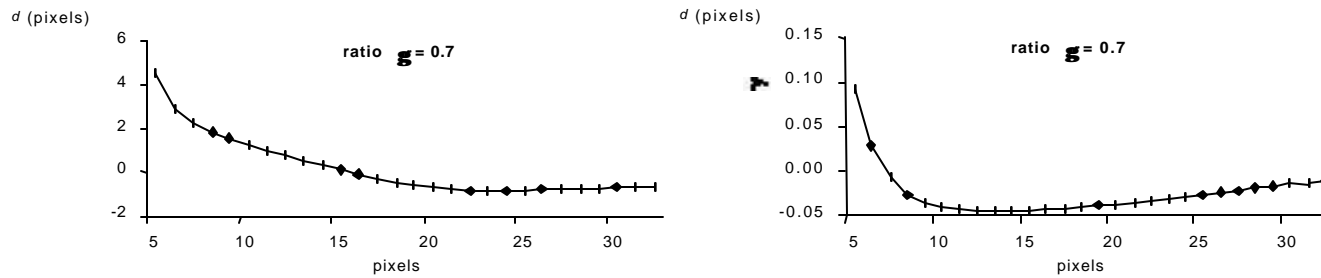


Figure 4: Results of the experiments with simulated dots with the Gaussian model for the Zeiss microscope parameters and including Poisson noise. Left: Discarding cases where $\xi < 0.1$. Right: Discarding cases where $\xi < 0.4$. Distances in pixels are in interpolated space. Note the different vertical scales.



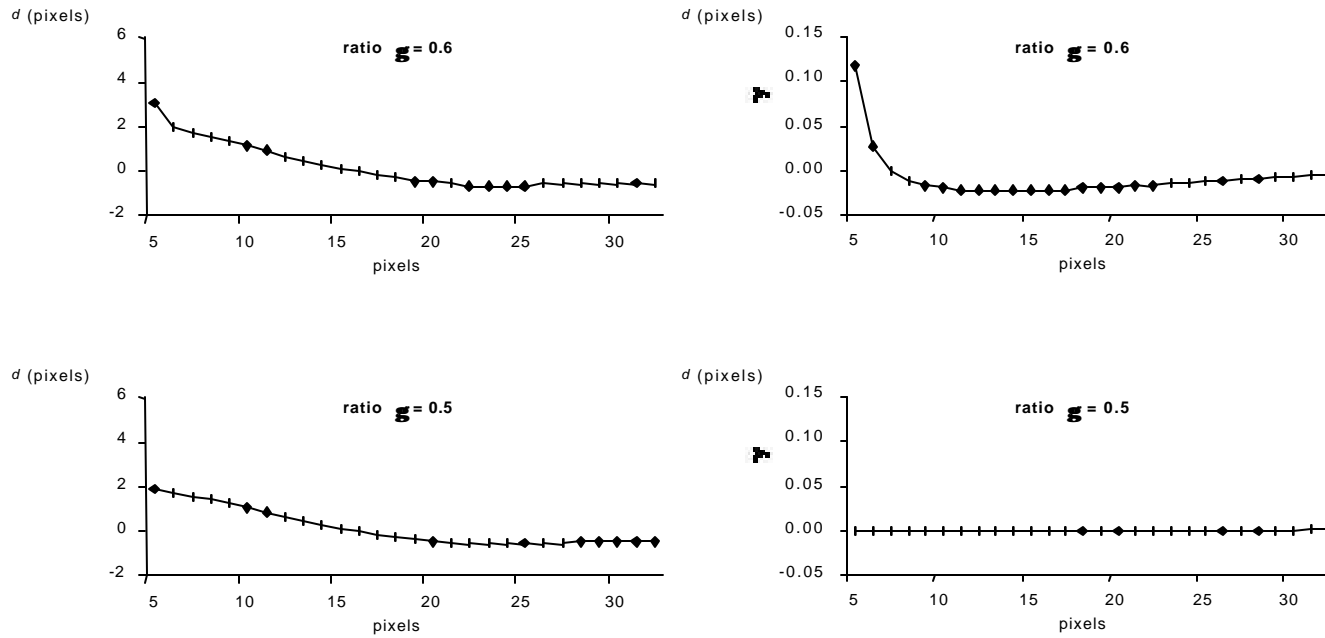


Figure 5: Simulated dots without noise. Error in the distance estimation and the peak ratio estimation for three values of the true peak ratio $\gamma = 0.7$ (above), $\gamma = 0.6$ (middle), and $\gamma = 0.5$ (below).